applied sciences

MDPI

Article

On the Cycle Stability and Macroscopic Structure of Iron Oxide Pellets for Thermochemical Hydrogen Storage: Influence of Water Content during the Pelletizing Process

Lea Huber [1,2,†], Melanie Heindl [1,†], Marc Schlosser [2], Arno Pfitzner [2] and Belal Dawoud [1,*]

[1] Laboratory of Sorption Processes, Faculty of Mechanical Engineering, East Bavarian Technical University of Applied Sciences Regensburg (OTH-Regensburg), Galgenbergstraße 30, 93053 Regensburg, Germany; lea2.huber@oth-regensburg.de (L.H.); melanie.heindl@st.oth-regensburg.de (M.H.)

[2] Institute of Inorganic Chemistry, University Regensburg, Universitätsstraße 31, 93053 Regensburg, Germany; marc.schlosser@chemie.uni-regensburg.de (M.S.); arno.pfitzner@chemie.uni-regensburg.de (A.P.)

* Correspondence: belal.dawoud@oth-r.de; Tel.: +49-941-943-9892

† These authors contributed equally to this work.

Abstract: Hydrogen storage based on the repeated reduction and oxidation (redox) reactions of iron oxide/iron composites represents a promising technology. This work is dedicated to studying the influence of the amount of water added during the pelletizing process on the cycle stability and structure of iron oxide pellets. The storage composites were prepared from iron oxide (Fe_2O_3) and 10 wt.-% support material (cement) with different amounts of water (18 and 33 wt.-%) in a laboratory-scale pelletizing disk. To evaluate the cycle stability of the composites, the kinetics of the redox reactions were experimentally measured at 800 °C in an atmosphere of 50% N_2 and 50% H_2 (reduction) or 50% steam (oxidation), respectively. Moreover, the structure of the pellets was analyzed by micro-computed tomography scans. It turned out that pellets with higher water contents attained faster kinetics and a higher cycle stability. The sample with the least water content (18 wt.-%) needed about 26 min and 19 min to reach a conversion rate of 80% during the reduction and oxidation reactions of the sixth redox cycle, respectively. In contrast, the sample with the highest water content (33 wt.-%) could achieve the same conversion rate after 18 min (reduction) and 13 min (oxidation) during the ninth redox cycle.

Keywords: hydrogen storage; redox reactions; iron/iron oxide; pelletizing process; cycle stability; water content

check for updates

Citation: Huber, L.; Heindl, M.; Schlosser, M.; Pfitzner, A.; Dawoud, B. On the Cycle Stability and Macroscopic Structure of Iron Oxide Pellets for Thermochemical Hydrogen Storage: Influence of Water Content during the Pelletizing Process. *Appl. Sci.* **2023**, *13*, 6408. https://doi.org/10.3390/app13116408

Academic Editors: Claudio Pistidda and Julian Jepsen

Received: 19 March 2023
Revised: 14 May 2023
Accepted: 21 May 2023
Published: 24 May 2023

Copyright: © 2023 by the authors. Licensee MDPI, Basel, Switzerland. This article is an open access article distributed under the terms and conditions of the Creative Commons Attribution (CC BY) license (https://creativecommons.org/licenses/by/4.0/).

1. Introduction

To achieve global greenhouse gas reduction targets, it is necessary to force a rapid transition from fossil fuels to a renewable-energy-based energy supply. However, when increasing the rate of utilization of renewable energies from wind and solar, their weather and seasonal dependencies do represent a technical challenge [1,2]. Their temporal variations in electricity production and consumption therefore raise the need for effective, affordable, and safe storage systems.

One emission-free opportunity to store surpluses of renewable electricity is to transform it into green hydrogen. To this aim, surplus renewable electrical energy can be utilized to split water into hydrogen and oxygen by an electrolyser. Green hydrogen can thus be stored and reused as soon as the energy demand increases. In a fuel cell or a hydrogen combustion engine connected to a generator, it can be converted back into electricity and heat. Hydrogen, as a cross-sector energy carrier, can also be used to decarbonize the transport and chemical sectors [3,4].

The storage of hydrogen at reasonable energy densities provides economic and technical challenges, because of its low density. Indeed, at atmospheric pressure conditions,

hydrogen has a low energy density of 0.0033 kWh l^{-1}. The current state-of-the-art methodologies to increase its volumetric energy density are to compress or liquefy hydrogen. At compressions of 350 and 700 bar, a volumetric energy density of 0.792 and 1.32 kWh l^{-1} can be reached, respectively. The second form of hydrogen storage technology is in the form of liquefied hydrogen. To liquify hydrogen, it has to be cooled down to about −253 °C, which represents the boiling point of hydrogen (−252.9 °C or 20.3 K). The simplest liquefaction process is the so-called Linde cycle, in which pure hydrogen is compressed and cooled down, e.g., by liquid nitrogen. The compressed, cold, and non-condensed gas is forced to pass through an adiabatic throttling valve. The result is a saturated liquid–vapour mixture, which is typically formed at a temperature of −253 °C. "The liquid hydrogen is collected as the desired product, and the vapor is routed through a heat exchanger to cool the compressed gas on its way to the throttling valve" [5]. The obtained liquefied hydrogen is then stored in vacuum-insulated cryogenic tanks. In the case of liquid H_2, the volumetric storage density amounts to about 2.3 kWh l^{-1} [4–8].

In addition to the above-mentioned physical storage technologies, hydrogen can also be chemically stored. Currently, a way to store hydrogen chemically in liquid form is to use liquid organic hydrogen carriers (LOHC). In the exothermic charging phase (hydrogenation), unsaturated organic compounds are hydrated at an elevated temperature and pressure. The endothermic dehydrogenation of the saturated, hydrogen-rich compounds (discharging) also requires an elevated temperature and a slightly increased pressure. Due to the low boiling point of LOHC materials, in most cases, the hydrogen has to be purified after dehydrogenation. In addition, typically, a catalyst is used in both charging and discharging. The process conditions and the storage density strongly depend on the used organic carrier material. In the case of N-ethylcarbazole [9,10], the hydrogenation typically takes places at a temperature between 130–160 °C and a pressure of about 70 bar. To release the hydrogen, a temperature of 200–230 °C and a slight overpressure is usually needed. With this N-ethylcarbazole, a storage density up to 5.8 wt.-% can be achieved [11,12].

Hydrogen can also be bonded onto solid materials. Due to their capability to strongly bind hydrogen, metals are often used as carrier materials (metal hydrides). In the exothermic charging phase, the adsorption of hydrogen into the metal lattice takes place. Due to the exothermic reaction, the temperature increases during charging. This shifts the reaction equilibrium towards higher pressures and leads to a decreased storage capacity unless the storage tank is cooled. The stored hydrogen can be released from the metal hydride during the desporption phase (endothermic discharging). The process temperature and pressure depend on the properties of the used metal/metal hydride, especially the absorption/desporption properties [4,13]. Metal hydrides such as magnesium hydride (MgH_2) can reach a high storage density of about 6 wt.-% (theoretically 7.6 wt.-%). A temperature of about 300 °C and a pressure of 30 bar must be applied for charging, whereas the discharging temperature is about 350 °C [14].

A promising approach for hydrogen storage is represented by the thermochemical reduction and oxidation (redox) of metal oxides (M_nO_m)/metals (M). In such a hydrogen storage process, hydrogen is not chemically stored within the metal bulk. Instead, hydrogen reduces the metal oxide to metal and is oxidized to steam (H_2O). Due to its high availability, low cost, and thermodynamic behavior, iron is considered to be the most suitable oxide carrier material [15]. The basis of the iron redox storage process was developed in the early 20th test century with the so-called "steam-iron" process, which was developed to produce hydrogen with a high purity and established on an industrial scale [16,17]. In the redox storage process, iron oxide/iron is repeatedly reduced and oxidized at atmospheric pressure conditions in a hydrogen and a steam gas stream, respectively. During the charging, iron oxide (magnetite, Fe_3O_4) is first reduced to wuestite (simplified as FeO). In the next step, it is further reduced to elemental iron (Fe). During this process, oxygen (O_2) is removed from the iron oxide and reacts with hydrogen (H_2) to create steam (H_2O). The discharging represents the reverse process in a steam atmosphere, where iron is oxidized back to iron oxide (see Equations (1) and (2)). To obtain a higher reaction speed, the redox reaction takes

place in a temperature range between 600 and 800 °C. Due to the process temperature and an oxygen partial pressure (p_{O_2}) of less than 10^{-14} bar, hematite (Fe_2O_3) cannot be formed, i.e., Fe_3O_4 cannot be oxidized to Fe_2O_3 by water vapor [18–22]. The absence of elementary hydrogen in the charged system represents a major safety advantage in comparison with the state-of-the-art technologies. In addition, redox storage systems can achieve a high volumetric energy density of about 2.8 kWh l_{bulk}^{-1} [23].

$$Fe_3O_4 + H_2 \rightleftharpoons 3\,FeO + H_2O \tag{1}$$

$$3\,FeO + 3\,H_2 \rightleftharpoons 3\,Fe + 3\,H_2O \tag{2}$$

However, the repeated redox reactions usually result in aging effects, such as the compaction of the porous storage material. As a consequence, the reactive surface area decreases, and the gas diffusion of the reacting gas slows down. This implies a reduction in the energy storage capacity and an increase in the reaction time, which is considered as a decrement in cycle stability. To improve the cycle stability, support materials can be added [15,24].

Several researchers in the field of chemical looping (CL) processes [25–27], solid oxide fuel cells (SOFC), and oxide ceramic batteries (ROB) [15,28,29] have shown that this aging can be reduced by the addition of supporting materials, e.g., silica, alumina, or calcium oxide. An improvement of both reaction kinetics and cycle stability during the redox storage process by adding different support materials was also proven in our previous work [30]. Therein, the pure iron oxide sample already required nine times more time for the second reduction compared to the first reduction. Furthermore, only 35% of the initial redox potential could be achieved in the third oxidation cycle. In contrast, the sample with 10 wt.-% support material lost only 5% of its redox potential after nine redox cycles. In addition, two different sintering temperatures, namely 950 and 1100 °C, were selected to investigate the influence of sintering temperature on the reaction kinetics of storage samples. The results showed that the reaction kinetics of samples with the higher sintering temperature of 1100 °C was strongly reduced. Already in the first oxidation cycle, this sample was nine times slower than the sample sintered at 950 °C. Furthermore, the redox reaction kinetics was measured at two constant temperatures (800 and 700 °C). Compared to the results obtained at 700 °C, the sample tested at 800 °C exhibited faster aging, with the reaction time being more strongly increased with the number of redox cycles. For example, a factor of nine between the reaction time needed at 700 °C and 800 °C for the eighth oxidation was observed [30].

This work represents a continuation of our previous publication [30] and describes the manufacturing process of the redox pellets in a lab-scale pelletizing disk. First, we analyzed the influence of the disk inclination angle and the rotational speed on the pellet shape. The core of the experimental work is dedicated, however, to the investigation of the influence of the amount of added water during the pelletizing process on both cycle stability and structure of the pellets. Based on the results obtained in [30], we used a temperature of 950 °C for sintering the samples and an amount of 10 wt.-% support material. In [30], a temperature of 800 °C resulted in rapid aging during cycling. Thus, the effects of various parameters on cycle stability and reaction kinetics can be seen in less than nine cycles. Therefore, a cycle temperature of 800 °C was chosen in this work. To investigate the structure of the samples before and after several redox cycles, micro-computed tomography scans have been conducted. In addition, the total open porosity of the samples has been investigated.

2. Material and Methods

As described before, the storage composites were manufactured with 90 wt.-% iron oxide (Fe_2O_3) and 10 wt.-% support material (cement). This ratio of 9:1 was chosen in order to maintain a high amount of the reactive storage material (iron oxide). In our previous

publication [30], we already presented the difference between having 0 wt.-% (pure iron oxide) and 10 wt.-% support material on the redox cycle stability.

2.1. Manufacturing Process

The manufacturing of the iron oxide pellets follows a three-stage process. In the first stage, iron oxide and the support material are dried at 105 °C for 24 h and mixed in a double cone laboratory mixer (J. Engelsmann AG, Ludwigshafen, Germany) for 60 min at a rotation speed of 50 min^{-1}(100% power of the mixer). After this stage, the pelletizing disk (illustrated in Figure 1) is applied to produce the so-called green pellets. Due to the rotation of the pelletizing disk and the alternating dosing of the powder mixture and water, agglomerated green pellets are formed. The internal structure of the pellets is affected by the way the pellets form, e.g., their coalescence, breakage, and abrasion transfer, which directly influences both the mechanical strength and the porosity of the pellets [31–33].

The inclination angle β is the angle between the surface of the pelletizing disk and the horizontal. The literature recommends keeping this angle between about 40 and 60° [31,32,34,35].

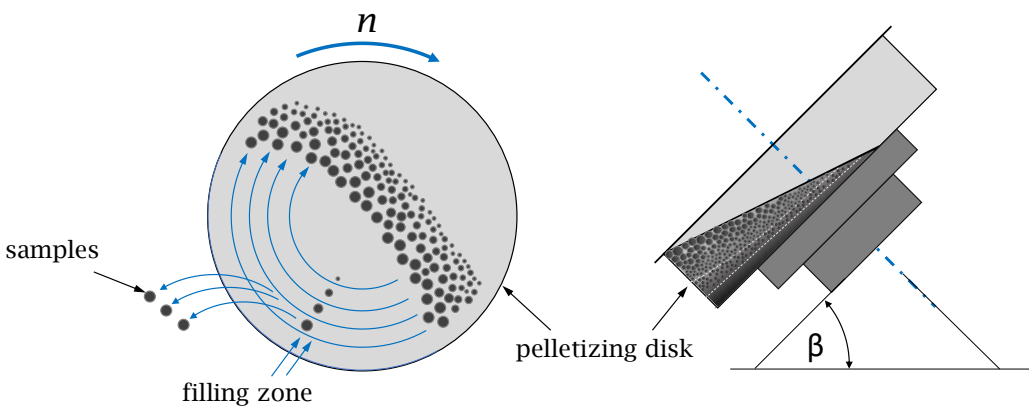

Figure 1. Schematic view of the pelletizing disk for the production of the storage composites (inspired by [34]), including the rotation speed (n), the disk angle (β), and the filling zone where water and powder mixture are added.

In a dedicated investigation campaign on the influence of β on the shape of the manufactured pellets, different angles were tested within the range between 30 and 65°. It turned out that, with β lower than 35°, the pellets tended to have an oval shape. With β between 50 and 60°, almost spherical pellets could be formed. Further increasing β above 60° led to increased material loss due to more ejection of the material from the pelletizing disk during rotation. Accordingly, β was set to 52° during the manufacturing of all produced and tested samples in this work.

The optimum rotation speed n_{opt} of the pelletizing disk was defined by [34,35] as in the range between 0.6 to 0.75 of the critical speed n_c. The latter can be obtained by setting equal the centrifugal and weight forces acting on the material during the rotation of the pelletizing disk. Solving the resulting equation for the rotational speed yields Equation (3), in which g represents the gravitational acceleration in m s^{-2}, β represents the inclination angle in °, and D_{Disk} represents the diameter of the pelletizing disk in m.

$$n_c = \frac{1}{\pi}\sqrt{\frac{g \cdot sin(\beta)}{2 \cdot D_{Disk}}} \tag{3}$$

The laboratory pelletizing disk has a diameter of 0.4 m. Considering the previously set inclination angle of 52°, the optimum rotation speed n_{opt} is estimated to be in the range between 35.6 and 44.5 min^{-1}. During our preliminary pelletizing runs, the rotation speed was set between about 35 and 40 min^{-1}. Within this range, no influence on the stability or on the shape of pellets could be identified.

As mentioned before, water dosing takes place alternately with the dosing powder mixture during the pelletizing process. In order to determine the amount of water that exists in the green pellets, the difference between the mass of the pellets immediately after being pelletized (wet green pellets) and after drying was measured. Thereby, the mass of the wet green pellets represents the 100% reference mass. The lowest amount of water by which pellets could still be formed was 18 wt.-%, while an amount of more than 33 wt.-% led to less stable and deformed wet pellets. Accordingly, pellets with a water amount between 18 and 33 wt.-% were produced and investigated.

The last manufacturing step is the sintering of the dried samples to increase their mechanical strength. The sintering temperature was selected to be higher than the maximum process temperature during the redox reactions in order to minimize the possibility of having the samples being sintered during the redox reactions. According to the results of our previous investigations [30], the sintering temperature was set to 950 °C.

In Table 1, the abbreviations of the produced and investigated samples are listed, along with the water content (wc) and the sample mass after sintering, which represent the initial mass of the pellets before the first reduction reaction (m_{start}).

Table 1. Production parameters of the investigated samples with the initial sample mass after sintering (m_{start}) and the water content (wc).

No.	P1	P2	P3	P4	P5	P6	P7	P8	P9	P10
wc/wt.-%	18	20	21	25	26	27	27	33	33	33
m_{start}/g	1.47	1.34	1.45	1.44	1.37	1.35	1.38	1.43	1.37	1.37

2.2. Experimental Setup

Figure 2 illustrates the experimental setup for cycling the produced storage pellets and investigating their kinetic performance during the repeated redox reactions. The core component of the setup was the simultaneous thermal analyzer (STA 449 Jupiter F3, Netzsch, Selb, Germany). The supply of hydrogen and nitrogen, as a carrier gas, could be regulated in the range of 0 to 250 mL min^{-1} ± 0.5% through a mass flow control (MFC) device for each gas. Moreover, a steam generator (aSTEAM DV2, aDROP) was applied to produce the required steam during the oxidation reaction. The amount of steam could be set within a range from 0 to 25 g h^{-1} with an accuracy of 1%. The accuracy of the weight measurement by the STA device amounted to ±0.1 µg, while the temperature was adjustable within a tolerance limit of ±0.3 °C. All devices were connected to a computer for process control as well as data monitoring and recording.

The redox reactions were conducted with the use of a thermogravimetric (TG) analyzer device in an atmosphere of 50% nitrogen and 50% hydrogen (reduction) or 50% steam (oxidation). In order to achieve fast aging in the investigated samples (in less than nine redox cycles), the TG measurements were carried out at 800 °C [30].

To analyze the measured reaction kinetics, the conversion rate for the reduction ($\alpha_{red}(t)$) and oxidation ($\alpha_{ox}(t)$) was determined by Equations (4) and (5). Thereby, the time-dependent mass change of the sample ($\Delta m(t)$) was divided by the maximum mass change after a complete conversion ($m_{max} - m_{min}$). The maximum mass (m_{max}) represents the mass of the sample in the fully oxidized state (Fe_3O_4), considering the amount of the supporting material, while the minimum mass (m_{min}) is the wight of the pellet in its completely reduced state (Fe). Under the tested process conditions (800 °C, $p_{O_2} < 10^{-14}$ bar), hematite is not stable. This implies a difference between initial sample mass and measured maximum mass of about 3% [29,30]. A fixed data point at $\alpha_{red} = 0.8$ and $\alpha_{ox} = 0.8$ was chosen to compare the kinetic behavior of the tested storage samples.

$$\alpha_{red}(t) = \frac{m_{max} - m(t)}{m_{max} - m_{min}} \tag{4}$$

$$\alpha_{ox}(t) = \frac{m(t) - m_{min}}{m_{max} - m_{min}} \tag{5}$$

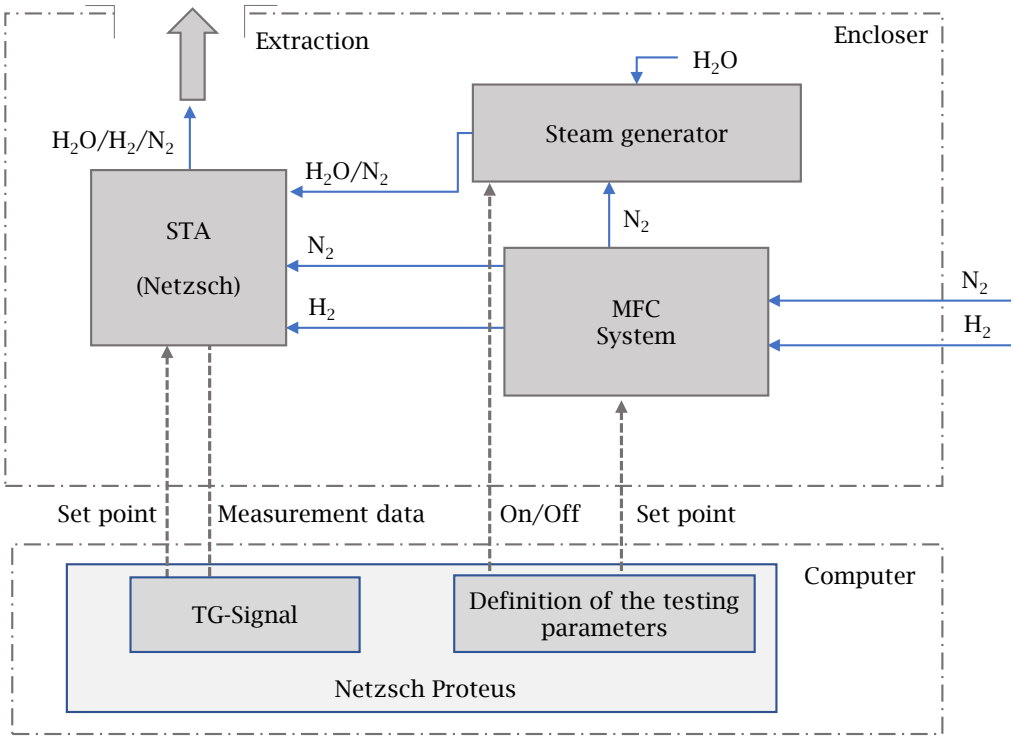

Figure 2. Schematic diagram of the experimental setup for the analysis of the reaction kinetics of the storage composites, including a simultaneous thermal analyzer (STA) connected to a steam generator and the mass flow controllers (MFC) to regulate the gas supply of hydrogen (H_2) and nitrogen (N_2). The operation parameters were defined, and the thermogravimetric (TG) signal was continuously evaluated via the Netzsch Proteus interface on the computer.

Furthermore, the structure of the cycled storage samples was investigated in a micro-computed tomography facility (µCT; Phoenix V | tome | x s240/180 from Waygate Technologies Digital Solutions Baker Hughes, Houston, TX, USA). The voxel size for the analysis was about 8 µm, and the number of images was 3000. The scanning parameters for the µCT scans were as follows: 140–160 kV voltage, 50–60 µA current, and 0.1 mm Cu filter. Reconstructed volumes were processed using the manufacturer's software phoenix datos | x 2 reconstruction 2.4.0. The software VG Studio Max 2022.2 from Volume Graphics was used to determine the parameters of the 3D images, including their surface area and volume.

To measure the open porosity of the samples (Φ), the volume of void space (V_v) was determined and divided by the total volume (V_{total}; see Equation (6)). To this aim, the density (ρ) of each sample was measured by a He-pycnometer (Pynomatic ATC, Thermo Fisher Scientific) with an accuracy of 0.01%. For the density measurements, the maximum standard deviation was about 0.3%. The total volume of the sample was estimated by the data from the µCT scans.

$$\Phi = \frac{V_v}{V_{total}} = 1 - \frac{m_{sample}}{\rho \cdot V_{total}} \tag{6}$$

3. Results and Discussion

As mentioned before, the storage samples were manufactured by varying the amount of added water between wc = 18 and 33 wt.-%. After sintering these samples, their reaction kinetics upon carrying out several redox cycles were measured by the TG analyzer. Moreover, the macroscopic structure of the samples was investigated using µCT scans, and

their open porosity was measured. The obtained results are presented and discussed in the following subsections.

3.1. Thermogravimetric Analysis

Table 2 summarizes the kinetic results, which are discussed in the following paragraphs, and presents the required time for the investigated samples to reach a conversion rate of α_{red} and $\alpha_{ox} = 0.8$ during reduction and oxidation.

Table 2. Time needed for each investigated sample (P1-P10) to reach a conversion rate of α_{red} and $\alpha_{ox} = 0.8$ in the second (red2, ox2), fifth (red5, ox5), sixth (red6, ox6) and ninth (red9, ox9) cycles, respectively. For comparison, the average reaction times of the three sample groups with a similar water content ($wc_1 \leq 20$ wt.-%, $wc_2 = 26$–27 wt.-%, $wc_3 = 33$ wt.-%) are included.

No.	wc /wt.-%	Red2 /min	Ox2	red5 /min	ox5	red6 /min	ox6	red9 /min	ox9
P1	18 (wc_1)	18	10	21	15	26	19		
P2	20 (wc_1)	17	9	20	14	24	18		
P3	21	18	10	19	12	20	13	27	17
P4	25	16	9	18	12	19	21		
P5	26 (wc_2)	15	8	16	10			22	14
P6	27 (wc_2)	16	9	16	10			23	16
P7	27 (wc_2)	16	9	17	10			24	15
P8	33 (wc_3)	15	8	17	10			20	14
P9	33 (wc_3)	14	8	16	10			18	14
P10	33 (wc_3)	15	8	16	10			22	12
	wc_1	18	10	21	14	25	18		
	wc_2	16	8	16	10			23	15
	wc_3	15	8	16	10			20	13

Figure 3 presents the time-dependent conversion rate ($\alpha(t)$) for the reduction and oxidation (Figure 3a,b) reactions during the second redox cycle.

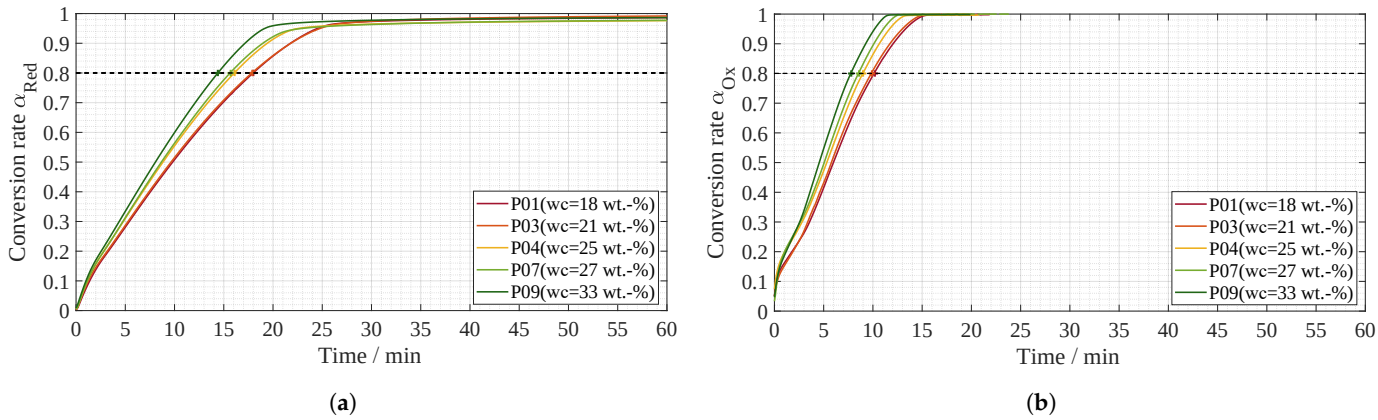

(**a**) (**b**)

Figure 3. (**a**) Reduction at 800 °C during the 2nd cycle. (**b**) Oxidation at 800 °C during the 2nd cycle. Measured conversion rate of samples with a different water content over time. Sample P9 with the highest water content (wc = 33 wt.-%) shows the highest kinetic performance, followed by samples P4 and P7 with wc = 25 wt.-% and wc = 27 wt.-%, respectively. The samples P1 and P3 with the lowest water contents (P1: wc = 18 wt.-%, P3: wc = 21 wt.-%) reached the marked conversion rate of $\alpha = 0.8$ (horizontal dashed line) last.

During the reduction, sample P9, with the highest water content (wc = 33 wt.-%), achieved the highest kinetic performance, as the conversion rate of $\alpha_{red} = 0.8$ was reached after 14 min, while samples P4 (wc = 25 wt.-%) and P7 (wc = 27 wt.-%) needed almost two more minutes to reach the same conversion rate. The samples with the lowest water

contents, P1 (wc = 18 wt.-%) and P3 (wc = 21 wt.-%), required as much as 18 min to achieve a conversion level of 80%.

A similar trend was observed during the oxidation. It can be first concluded that the oxidation reactions are notably faster compared to the reduction reactions. Indeed, sample P9 reached the 80% level after about 8 min, while samples P4 and P7 achieved the same conversion rate about 1 min later. Finally, the samples with the lowest water content (P1, P3) needed two minutes more to make it to $\alpha = 0.8$.

The results of the second redox cycle indicate that a higher water content during the pelletizing process leads to faster reaction kinetics. To determine the influence of the water content on the cycle stability, the conversion rate over several cycles was investigated. In the following discussions, the investigated samples were split into three categories depending on their water content, namely $wc_1 \leq 20$ wt.-% (Figure 4a,b), $wc_2 = 26$–27 wt.-% (Figure 4c,d), and $wc_3 = 33$ wt.-% (Figure 4e,f).

Figure 4a,b illustrates the time-dependent conversion rates of samples P1 and P2, which had the lowest water content of equal to or less than 20 wt.-% (wc_1). It is clear that the reduction reaction kinetics strongly decreases with the number of cycles (cf. $\alpha_{red} = 0.8$: $t_{red2-wc1} = 18$ min, $t_{red5-wc1} \approx 21$,min, and $t_{red6-wc1} \approx 25$ min). A similar behavior can be observed during the oxidation reactions (cf. α_{ox}=0.8: $t_{ox2-wc1} \approx 10$ min, $t_{ox5-wc1} \approx 14$ min, and $t_{ox6-wc1} \approx 18$ min). It is also observable that samples P1 and P2 cannot reach the complete oxidation conversion of $\alpha_{ox} = 1$ in 60 min. In addition, the reaction kinetics of both samples P1 and P2 during the sixth redox cycle is clearly slower than those of the samples with higher water contents during the ninth redox cycle (cf. $\alpha_{ox} = 0.8$: $t_{ox9-wc2} \approx 15$ min, and $t_{ox9-wc3} \approx 13$ min). Thus, no further cycles have been measured for P1 and P2.

In Figure 4c,d, the time-dependent conversion rates for the reduction and oxidation reactions of the samples P5, P6, and P7 (wc_2) during the second, fifth, and ninth cycles are illustrated. For those samples, the conversion rates during the second and the fifth reduction cycles are approximately the same ($\alpha_{red} = 0.8$: $t_{red2-wc2} \approx t_{red5-wc2} = 16$ min). In case of sample P5, $\alpha = 0.8$ can be reached about 1 min faster during the second cycle. Between the fifth and the ninth cycle, the time needed for α_{red} to reach 0.8 increases by 7 min. Additionally, for the samples P5, P6, and P7, the kinetics of the oxidation reactions were notably faster compared to the reduction reactions. Strictly speaking, the required time for the oxidation to reach $\alpha_{ox} = 0.8$ during the second, fifth, and ninth oxidation cycles is about 8 min, 10 min and 15 min, respectively.

In comparison to samples with the water contents wc_1 and wc_2, the conversion rates of samples P8, P9, and P10 (wc_3 in Figure 4e,f) exhibit a smaller decrease over the nine redox cycles, which is attributed to less aging effects. During the second redox cycle, the average reaction time to reach a conversion level of 80% is about 15 min for reduction and 8 min for oxidation, respectively. The time required to achieve an 80% conversion rate during the fifth redox cycle of the reaction is about 1 min longer for the reduction and 2 min longer for the oxidation reactions. Sample P10 is, on average, 3 min slower than P8 and P9 (cf. $\alpha_{red} = 0.8$: $t_{red9-P10} \approx 22$ min). Additionally, sample P10 cannot reach the complete conversion to $\alpha_{red} = 1$ in 60 min. However, during the ninth oxidation, sample P10 shows a comparable reaction behavior to P8 and P9 ($\alpha_{ox} = 0.8$: $t_{ox9-P8} \approx 14$ min, $t_{ox9-P9} \approx 14$ min, and $t_{ox9-P10} \approx 12$ min).

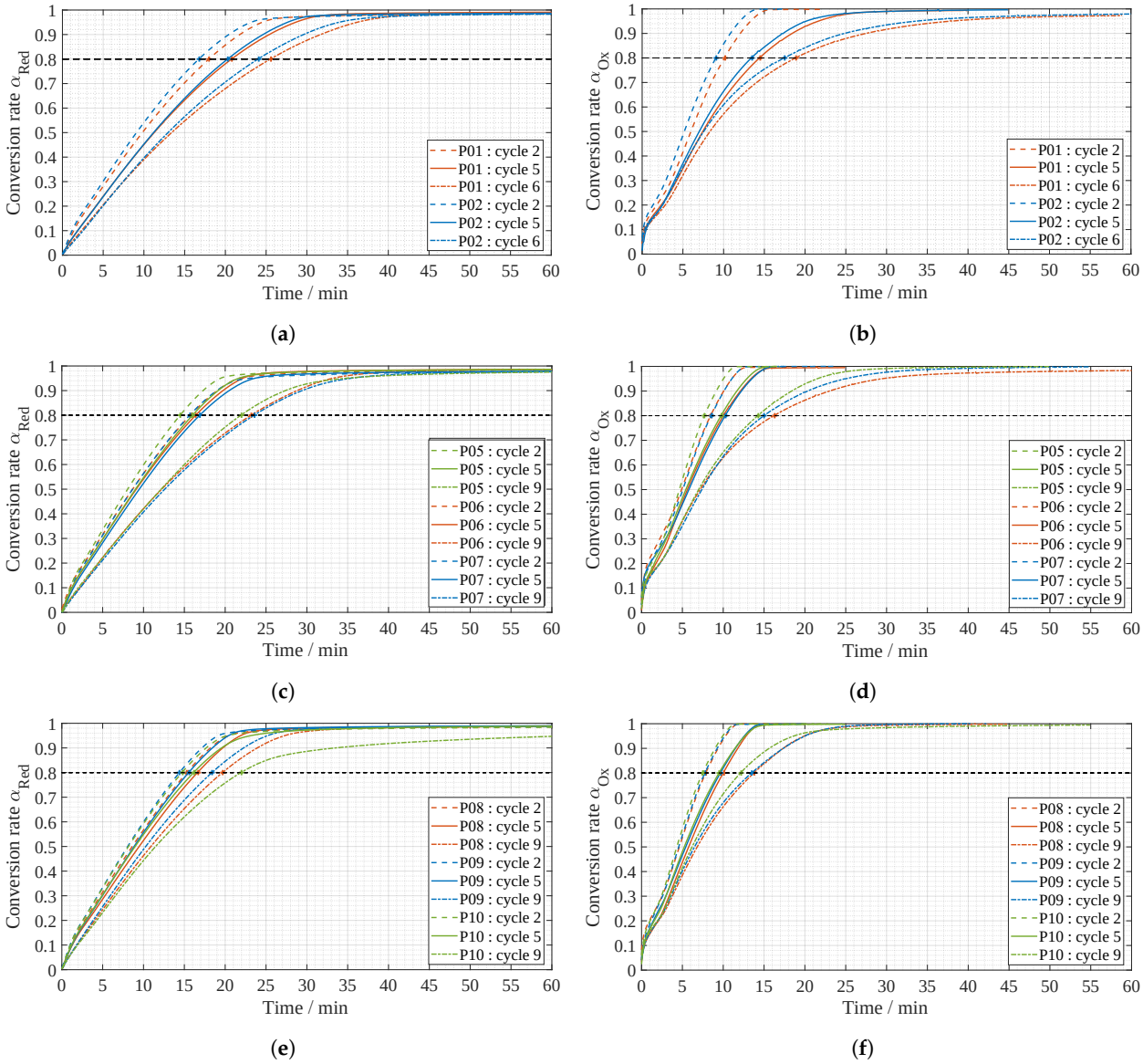

Figure 4. (**a**) Reduction of samples P1 and P2 ($wc_1 \leq 20$ wt.-%). (**b**) Oxidation of samples P1 and P2 ($wc_1 \leq 20$ wt.-%). (**c**) Reduction of samples P5, P6, and P7 ($wc_2 = 26$–27 wt.-%). (**d**) Oxidation of samples P5, P6, and P7 ($wc_2 = 26$–27 wt.-%). (**e**) Reduction of samples P8, P9, and P10 ($wc_3 = 33$ wt.-%). (**f**) Oxidation of samples P8, P9, and P10 ($wc_3 = 33$ wt.-%). Measured conversion rates over time of pellet samples with different water contents for the reduction and oxidation reactions during the 2nd, 5th, and 6th or 9th cycles at 800 °C. The conversion rate of α_{red} and $\alpha_{ox} = 0.8$ are marked with the dashed horizontal line in each diagram. The reaction kinetics of samples with a water content of equal or less then 20 wt.-% (wc_1) strongly decreased within six redox cycles. In contrast, the samples with higher water contents ($wc_2 = 26$–27 wt.-%, $wc_3 = 33$ wt.-%) could achieve a faster conversion rate during even nine redox cycles. The best results could be obtain with wc_3 samples. Samples with a similar water content (wc_1, wc_2, and wc_3) showed almost the same reaction behavior during the measured cycles, except for the ninth reduction cycle of sample P10.

The discussed results so far indicate that the samples with a higher water content ($wc_3 \approx 33$ wt.-%) have a higher cycle stability. To illustrate this conclusion more clearly, the conversion rates of sample P3 (wc = 21 wt.-%), P6 (wc = 27 wt.-%), P2 (wc = 20 wt.-%), and P9 (wc = 33 wt.-%) are compared in Figure 5.

In the following, the relative increase in reaction time during the redox cycles (illustrated in Figure 5) is discussed. Concerning sample P2, the time needed to reach $\alpha = 0.8$

increases from the second to the sixth cycle by 40% during the reduction reaction and 90% during the oxidation reaction. In contrast, sample P3 showed a higher cycle stability, with $t_{red6-P3} \approx 20$ min and $t_{ox6-P3} \approx 13$ min necessary to reach $\alpha = 0.8$ during the reduction and oxidation reactions, respectively. This is equivalent to a decrement of 10% in the reduction and 30% in the oxidation kinetics between the second and the sixth cycle. Between the second and the ninth cycle, the aging effect becomes more obvious as the decrement in the reduction kinetics amounts to 50% ($t_{red9-P3} \approx 27$ min), while the oxidation kinetics are reduced by 80% ($t_{ox9-P3} \approx 17$ min). In comparison, sample P6, with the medium water content of 27 wt.-%, reaches $\alpha = 0.8$ in about 23 min during the 9th reduction and 16 min during the 9th oxidation. Compared with the second redox cycle, a decrement in the kinetic performance of 50% for the reduction and 90% for the oxidation reaction can be determined.

Indeed, sample P9, with the highest water content (33 wt.-%), showed the highest reduction and oxidation kinetics and cycle stability (cf. $t_{red2-P9} \approx 14$ min, $t_{red9-P9} \approx 18$ min; $t_{ox2-P9} \approx 8$ min, $t_{ox9-P9} \approx 14$ min). This implies an increase in the reaction time of 20% and 60% regarding the second and ninth reduction and oxidation cycles, respectively.

The rather large difference in the performance of sample P3 with 21 wt.-% compared to sample P2 with 20 wt.-% of water content indicates that the water content might have a dominant effect on the reaction kinetics and the cycle stability as the key performance indicators (KPIs). However, other factors, such as the sample structure, may also influence both KPIs. Accordingly, further investigations regarding the influence of the micro structure of the investigated samples on the reaction kinetics and cycle stability were carried out. The results of theses investigations are documented and discussed in the following section.

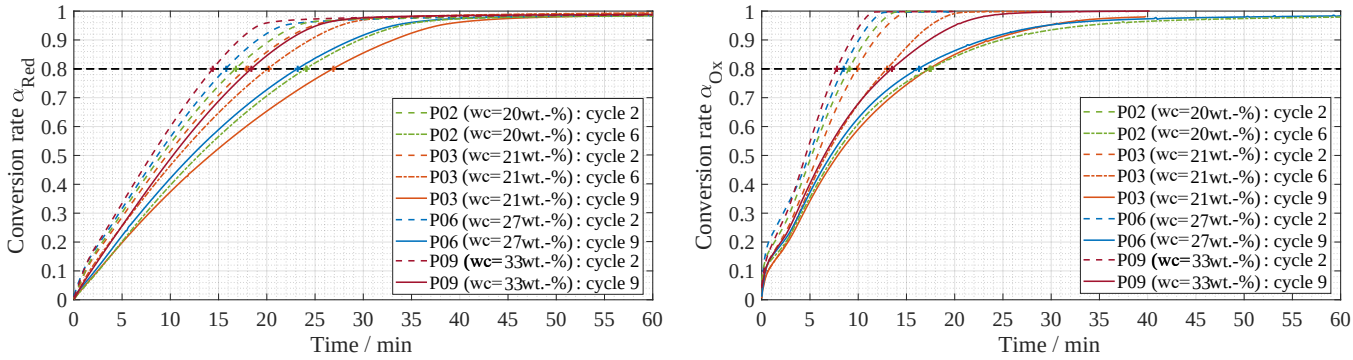

(**a**) (**b**)

Figure 5. (**a**) Reduction at 800 °C. (**b**) Oxidation at 800 °C. Measured conversion rates over time of the samples P2, P3, P6, and P9 with different water contents during the reduction and oxidation reactions in the 2nd, 6th, or 9th redox cycle at 800 °C. The dashed horizontal lines mark the conversion rates of α_{red} and $\alpha_{ox} = 0.8$ in each diagram. Comparing the conversion rates of the different samples shows that with increased water content, the samples attain a higher conversion rate and a higher cycle stability. Despite the similar water content of samples P2 (wc = 20 wt.-%) and P3 (wc = 21 wt.-%), sample P3 achieved a clearly higher conversion rate and cycling stability.

3.2. Structural Investigations

In the flowing µCT scans, the areas with no storage material (only air) are marked in black. Gray areas represent the material of the storage samples. The brightness of the parts is an indicator of their density [36]. For iron oxide samples, a higher brightness can be attributed to areas with a more dense structure or material with a higher density, e.g., iron compared to iron oxide particles. Due to the fully oxidized state of the investigated samples, it is assumed that areas with higher brightness are areas with a more dense structure. Through µCT scans, the internal macroscopic structure of the samples can be obtained without the necessity of destroying them, which makes it possible to study the sample structure before and after cycling.

In Figure 6, the μCT images of the samples with the lowest water contents (≤21 wt.-%), namely P1 and P2 after the sixth redox cycle, as well as P3 after the ninth cycle, are presented. In particular, the internal structure of sample P1 (wc = 18 wt.-%; Figure 6a) exhibits separated spherical areas with material accumulations (≈ 0.1–1.8 mm) and cavities in between. On the other hand, the outermost shell appears as a continuous dense layer. Sample P2 shows also an agglomerated internal structure (Figure 6b). In contrast to sample P1, a higher amount of smaller agglomerates with a diameter of about 0.3 mm can be recognized. Accumulations up to about 1.3 mm can also be observed. Compared to sample P1 and P2, sample P3 shows less and smaller material accumulations ≤ 0.3 mm, which appear around a porous core (see Figure 6c). However, a dense exterior shell also forms after the ninth redox cycle.

The obtained results indicate that the agglomerated structure and the formation of an outward dense layer lead to the presented slowdown of the reaction kinetics. This is caused by the correlated less effective gas transport of H_2 or H_2O towards the sample structure during the reduction and oxidation reactions, respectively. These results are in line with our previously published results [30] as well as [15,37].

To verify the suggestion of a structure with a higher density, the open porosity Φ of the investigated samples was determined according to Equation (6). This measuring campaign resulted in an open porosity of about 23% (P1: wc = 18 wt.-%), 25% (P2: wc = 20 wt.-%) and 31% (P3: wc = 21 wt.-%). Compared to the open porosity of the other samples, the named three samples acquire the lowest porosities (cf. Table 3). Furthermore, sample P3 after the ninth redox cycle does record a higher porosity than samples P1 and P2 after six cycles. This is consistent with the observed higher kinetics and cycle stability of sample P3. The results of the μCT scans in combination with the determined porosity indicate that the cavities inside the internal structure of samples P1 and P2 are mostly closed and barely contribute to the enhancement of the reaction kinetics [38].

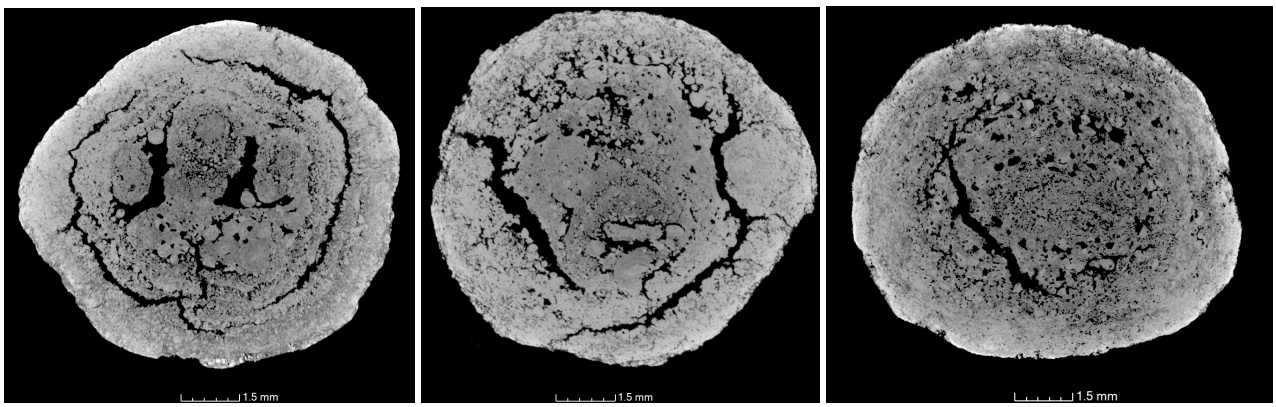

(**a**) (**b**) (**c**)

Figure 6. (**a**) Sample P1 (wc = 18 wt.-%) after the 6th cycle, (**b**) sample P2 (wc = 20 wt.-%) after the 6th cycle, (**c**) sample P3 (wc = 21 wt.-%) after the 9th cycle. Micro-computed tomography scans of samples P1, P3, and P2 after several redox cycles. The μCT scans of samples P1 and P2 exhibit separated spherical ares with material accumulations and large cavities in the interior part. Sample P3 shows comparably smaller accumulations. After six (P1, P2) or nine (P3) redox cycles, the formation of a dense external shell can be observed.

Figure 7 illustrates the μCT images of the samples P5 and P7 after nine redox cycles. The structure also shows internal cracks and the formation of an external shell with a higher density compared to the interior. However, the storage material of the samples is nearly homogeneously distributed without agglomerations, such as in sample P1.

The average porosity is about 35% (cf. Table 3). This suggests that increasing the added water amount during the pelletizing process from about 20 to 27 wt.-% does have a positive effect on the sample's structure.

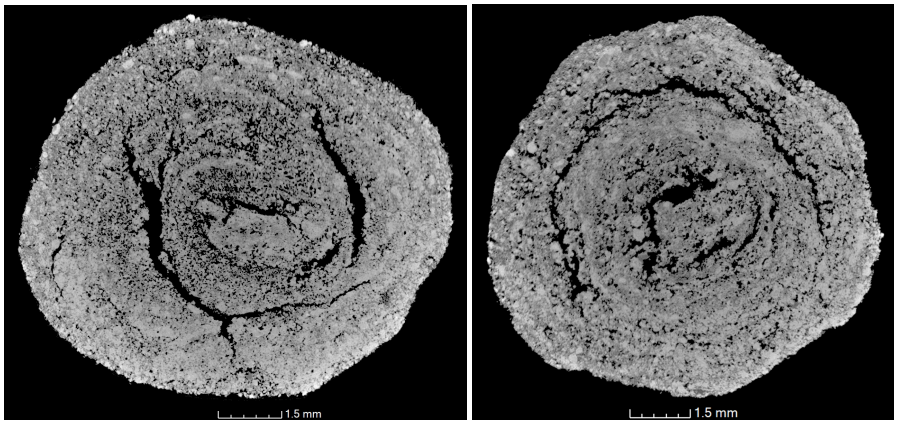

(**a**) (**b**)

Figure 7. (**a**) Sample P5 (wc =26 wt.-%) after the 9th cycle; (**b**) sample P7 (wc = 27 wt.-%) after the 9th cycle. Micro-computed tomography scans of sample P5 and P7 after nine redox cycles, which illustrate the formation of a compact exterior shell, larger cavities, and a nearly homogeneous distribution of storage material and pores.

The µCT images of samples P8, P9, and P10 with the highest water contents of 33 wt.-% (see Figure 8) display a homogeneous distribution of storage material and pores. Furthermore, the formation of cracks can be seen, which extend from the outside shell towards the internal structure. Compared to the other investigated samples in Table 3, samples P8, P9, and P10 reach the highest porosity, with an average of about 44%. The visualized internal structure of the samples along with the higher total porosities indicate an increased specific reaction surface, which positively affect the reaction kinetics upon improving the gas transport rates.

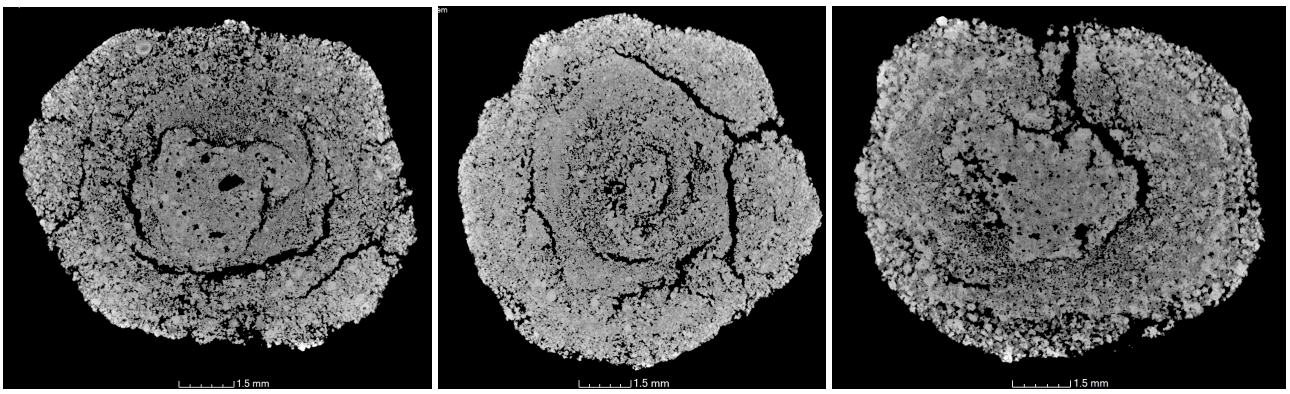

(**a**) (**b**) (**c**)

Figure 8. (**a**) Sample P8 (wc = 33 wt.-%) after the 9th cycle, (**b**) sample P9 (wc = 33 wt.-%) after the 9th cycle, and (**c**) sample P10 (wc = 33 wt.-%) after the 9th cycle. Micro-computed tomography scans of samples P8, P9, and P10 after nine redox cycles. The structure of the samples display the formation of cracks and a homogeneous distribution of storage material and pores.

Table 3. Open porosities Φ of the investigated samples after the TG analysis, calculated according to Equation (6). The samples P1 (wc = 18 wt.-%) and P2 (wc = 20 wt.-%) were measured after six redox cycles. The open porosities of samples P3 (wc = 21 wt.-%), P5 (wc = 26 wt.-%), P7 (wc = 27 wt.-%), P8, P9, and P10 with wc = 33 wt.-% were determined after nine redox cycles.

No.	P1	P2	P3	P5	P7	P8	P9	P10
Φ/%	23	25	31	35	35	46	42	45

In addition to the µCT scans after six or nine cycles, the structures of the samples P2, P5, and P8 were investigated right after the sintering phase and before the start of the redox cycling tests. The obtained results are depicted in (Figure 9).

In Figure 9a, the formation of a dense outer shell and the agglomerated internal structure of sample P2 is already visible. This indicates that these pellets were formed primarily by the coalescence of compressed agglomerates. A reason for this could be the small amount of added water, since agglomerates with a low moisture content are comparatively more brittle, leading to more frequent breakage and abrasion [32,34].

With further cycling, the cavities in the internal structure expand (cf. Figures 6b and 9a), which is assumed to take place because of the increasing sintering effects of iron/iron oxide during the repeated redox cycles. Figure 9b demonstrates that an increased water content has a positive effect on the distribution of storage material and small pores during the pelletizing process.

Figure 9c illustrates the initial structure of sample P8 with the highest added water amount of 33 wt.-%. Compared to sample P2 and P5, sample P8 shows a much higher porosity, most specifically in the outermost layers. The results indicate that a higher open porosity can be generated by adding a larger amount of water during the pelletizing process.

Indeed, all investigated samples have shown visible aging effects. Compared to the µCT images before the redox cycling, a more compact structure is formed after few redox cycles, especially in the outermost layers. The sintering effect due to the execution of the redox cycles at 800 °C can also be determined when comparing the sample volume of the initial (V_{start}) and the re-oxidized (V_{redox}) samples. In fact, the volume of sample P2 is reduced from $V_{start_{P2}} = 630\,\text{mm}^3$ down to $V_{redox_{P2}} = 387\,\text{mm}^3$, while the sample P5 contracts from $V_{start_{P5}} = 1064\,\text{mm}^3$ to $V_{redox_{P5}} = 452\,\text{mm}^3$. Considering the sample P8, it is reduced from $V_{start_{P8}} = 1180\,\text{mm}^3$ to $V_{redox_{P8}} = 571\,\text{mm}^3$ after nine redox cycles.

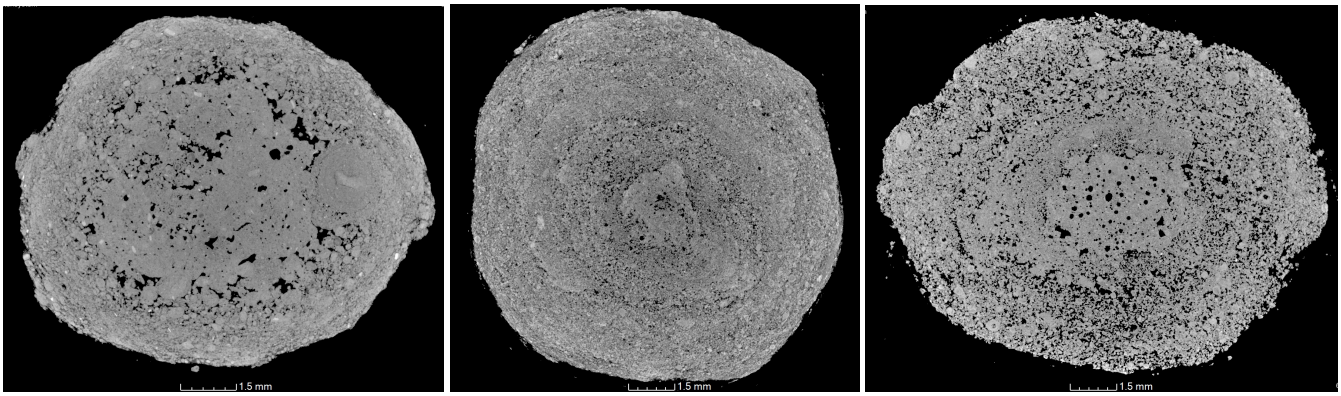

(**a**) (**b**) (**c**)

Figure 9. (**a**) Sample P2 (wc = 20 wt.-%) after sintering. (**b**) sample P5 (wc = 26 wt.-%) after sintering. (**c**) sample P8 (wc = 33 wt.-%) after sintering. Micro-computed tomography scans of the samples P2, P5, and P8 after sintering. The structure of sample P2 displays a dense external shell and the formation of accumulations in its interior already after the sintering process. The µCT scans of samples P5 and P8 show a homogeneous distribution of storage material and pores. Compared to sample P5, sample P8 exhibits a higher porosity.

Moreover, it is noticeable that the cracks within the sample structure are mostly in the shape of a shell, which can be attributed to the step-wise agglomeration of the storage material in layers during the applied pelletizing process.

The obtained results indicate that increasing the amount of added water during the pelletizing process results in a more homogeneous distribution and a higher open porosity of the produced pellet samples. This promotes faster reaction kinetics and an increased gas permeability [30,39,40].

The correlated higher reaction kinetics and cycle stability of the samples with higher water contents pave the way to more dedicated developments, in which the number of redox cycles over which the samples should remain stable must be increased to guarantee a promising practical application as a hydrogen storage material. In addition, the change in the microscopic structure and chemical phase composition due to the repeated reduction and oxidation of iron storage masses will be investigated in more detail. Furthermore, the mechanical stability of the samples in bulk will be tested as a prerequisite for studying the reaction kinetics of the storage sample in a lab-scaled iron redox reactor. The results of these development steps will be the subject of our subsequent publications.

4. Conclusions

In this work, the influence of the amount of water added during the pelletizing process on the redox cycle stability and on the reaction kinetics of iron oxide pellets was studied. To this aim, the water content was varied between wc = 18 to 33 wt.-%. After sintering at 950 °C, the reaction kinetics of the repeated reduction and oxidation at 800 °C was investigated. Furthermore, the micro-structure and the open porosity of the produced pellet samples were determined.

The obtained results indicate a direct correlation between the added water amount, the structure of the pellets, and their reaction kinetics. Pellets with a higher water content tend to have faster kinetics and a higher cycle stability. Considering the sixth redox cycle, sample P1 with the lowest water content of 18 wt.-% needed about 26 min and 19 min to reach a conversion rate of $\alpha = 0.8$ during the reduction and oxidation, respectively. In contrast, sample P10 with the highest water content of 33 wt.-% could achieve a similar conversion rate after only 18 min (reduction) and 13 min (oxidation) in the ninth cycle.

Micro-computed tomography scans before and after the redox cycling showed that samples with lower water contents are subjected to a more agglomerated internal structure with a dense outermost shell. In addition, sample P1 (wc = 18 wt.-%) showed the lowest open porosity of $\Phi_{P1} \approx 23\%$, compared to samples P8 and P10 (wc = 33 wt.-%) with the highest open porosities of $\Phi_{P8} \approx 46\%$ and $\Phi_{P10} \approx 45\%$, respectively. Furthermore, increasing the added water content resulted in a more homogeneously distributed pore structure. A homogeneous distributed pore structure and a higher porosity are associated with higher reaction kinetics and better cycle stability due to an increased specific reaction surface and gas permeability. Indeed, more development work is needed to approve the cycle stability over more redox cycles and to investigate the mechanical stability of the iron oxide pellets.

Author Contributions: Conceptualization, L.H.; methodology, L.H.; software, L.H. and M.H.; validation, L.H., M.H. and B.D.; formal analysis, L.H. and M.H.; investigation, L.H. and M.H.; resources, L.H., B.D. and A.P.; data curation, L.H. and M.H.; writing—original draft preparation, L.H.; writing—review and editing, M.H, B.D., A.P. and M.S.; visualization, L.H. and M.H.; supervision, B.D. and A.P. All authors have read and agreed to the published version of the manuscript.

Funding: The first author would like to acknowledge the funding received by the Nagelschneider Foundation.

Institutional Review Board Statement: Not applicable.

Informed Consent Statement: Not applicable.

Data Availability Statement: Data is contained within the article.

Acknowledgments: Both first and second authors would like to acknowledge the Regensburg Center of Energy and Resources (RCER) of OTH Regensburg. In addition, the authors woud like to gratefully thank both the Regensburg Center of Biomedical Engineering (RCBE) for the support through the use of their μCT facility and the Laboratory for Geotechnics of OTH Regensburg for the received support through the use of their He pycnometer facility.

Conflicts of Interest: The authors declare no conflict of interest.

References

1. Sterner, M.; Stadler, I. *Handbook of Energy Storage: Demand, Technologies, Integration*; Springer: Berlin/Heidelberg, Germany, 2019.
2. Aneke, M.; Wang, M. Energy storage technologies and real life applications—A state of the art review. *Appl. Energy* **2016**, *179*, 350–377. [CrossRef]
3. White, C.; Steeper, R.; Lutz, A. The hydrogen-fueled internal combustion engine: A technical review. *Int. J. Hydrogen Energy* **2006**, *31*, 1292–1305. [CrossRef]
4. Sreedhar, I.; Kamani, K.M.; Kamani, B.M.; Reddy, B.M.; Venugopal, A. A Bird's Eye view on process and engineering aspects of hydrogen storage. *Renew. Sustain. Energy Rev.* **2018**, *91*, 838–860. [CrossRef]
5. Zhang, J.Z.; Li, J.; Li, Y.; Zhao, Y. *Established Methods Based on Compression and Cryogenics*; John Wiley and Sons, Ltd: Hoboken, NJ, USA, 2014; Chapter 5, pp. 75–90. [CrossRef]
6. Klell, M. *Storage of Hydrogen in the Pure Form*; John Wiley and Sons, Ltd.: Hoboken, NJ, USA, 2010; Chapter 1, pp. 1–37. [CrossRef]
7. Kurzweil, P.; Dietlmeier, O.K. *Elektrochemische Speicher: Superkondensatoren, Batterien, Elektrolyse-Wasserstoff, Rechtliche Grundlagen*, 1st ed.; Springer: Wiesbaden, Germany, 2015. [CrossRef]
8. Hassan, I.; Ramadan, H.S.; Saleh, M.A.; Hissel, D. Hydrogen storage technologies for stationary and mobile applications: Review, analysis and perspectives. *Renew. Sustain. Energy Rev.* **2021**, *149*, 111311. [CrossRef]
9. Kiermaier, S.; Lehmann, D.; Bösmann, A.; Wasserscheid, P. Dehydrogenation of perhydro-N-ethylcarbazole under reduced total pressure. *Int. J. Hydrogen Energy* **2021**, *46*, 15660–15670. [CrossRef]
10. Teichmann, D.; Arlt, W.; Wasserscheid, P.; Freymann, R. A future energy supply based on Liquid Organic Hydrogen Carriers (LOHC). *Energy Environ. Sci.* **2021**, *4*, 2767–2773. [CrossRef]
11. Niermann, M.; Beckendorff, A.; Kaltschmitt, M.; Bonhoff, K. Liquid Organic Hydrogen Carrier (LOHC) – Assessment based on chemical and economic properties. *Int. J. Hydrogen Energy* **2019**, *44*, 6631–6654. [CrossRef]
12. Müller, Karsten. Technologies for the Storage of Hydrogen Part 1: Hydrogen Storage in the Narrower Sense. *ChemBioeng Rev.* **2019**, *6*, 72–80. [CrossRef]
13. Zhang, J.Z.; Li, J.; Li, Y.; Zhao, Y. *Chemical Storage Based on Metal Hydrides and Hydrocarbons*; John Wiley and Sons, Ltd.: Hoboken, NJ, USA, 2014; Chapter 6, pp. 91–119. [CrossRef]
14. Andersson, J.; Grönkvist, S. Large-scale storage of hydrogen. *Int. J. Hydrogen Energy* **2019**, *44*, 11901–11919. [CrossRef]
15. Menzler, N.H.; Hospach, A.; Niewolak, L.; Bram, M.; Tokariev, O.; Berger, C.; Orzessek, P.; Quadakkers, W.J.; Fang, Q.; Buchkremer, H.P. Power-To-Storage - The Use of an Anode-Supported Solid Oxide Fuel Cell as a High-Temperature Battery. *ECS Trans.* **2013**, *57*, 255–267. [CrossRef]
16. Huebler, J.; Johnson, J.L.; Schora, F.J.C.; Tarman, P.B. Production of Hydrogen via the Steam-Iron Process Utilizing Dual Solids Reycle. Application US3442619 (A), 6 May 1969.
17. Messerschmitt, A. Process of Producing Hydrogen. US971206 (A), 2 December 1908.
18. Gamisch, B.; Huber, L.; Gaderer, M.; Dawoud, B. On the Kinetic Mechanisms of the Reduction and Oxidation Reactions of Iron Oxide/Iron Pellets for a Hydrogen Storage Process. *Energies* **2022**, *15*, 8322. [CrossRef]
19. Young, D.J. *High Temperature Oxidation and Corrosion of Metals*, 2nd ed.; Elsevier: Amsterdam, The Netherlands, 2016.
20. El-Geassy, A.A. Gaseous reduction of Fe_2O_3 compacts at 600 to 1050 °C. *J. Mater. Sci.* **1986**, *21*, 3889–3900. [CrossRef]
21. Turkdogan, E.T.; Vinters, J.V. Gaseous reduction of iron oxides: Part I. Reduction of hematite in hydrogen. *Metall. Mater. Trans. B* **1971**, *2*, 3175–3188. [CrossRef]
22. Maier, H.J.; Niendorf, T.; Bürgel, R. *Handbuch Hochtemperatur-Werkstofftechnik: Grundlagen, Werkstoffbeanspruchungen, Hochtemperaturlegierungen und -Beschichtungen*, 6th ed.; Springer Vieweg: Wiesbaden, Germany, 2019. [CrossRef]
23. Gamisch, B.; Gaderer, M.; Dawoud, B. On the Development of Thermochemical Hydrogen Storage; An Experimental Study of the Kinetics of the Redox Reactions under Different Operating Conditions. *Appl. Sci.* **2021**, *11*, 1623. [CrossRef]
24. Brinkman, L.; Bulfin, B.; Steinfeld, A. Thermochemical Hydrogen Storage via the Reversible Reduction and Oxidation of Metal Oxides. *Energy Fuels* **2021**, *35*, 18756–18767. [CrossRef]
25. Voitic, G.; Hacker, V. Recent advancements in chemical looping water splitting for the production of hydrogen. *RSC Adv.* **2016**, *6*, 98267–98296. [CrossRef]
26. Ismail, M.; Liu, W.; Scott, S.A. The performance of Fe_2O_3-CaO Oxygen Carriers and the Interaction of Iron Oxides with CaO during Chemical Looping Combustion and H_2 production. *Energy Procedia* **2014**, *63*, 87–97. [CrossRef]
27. Liu, W.; Lim, J.Y.; Saucedo, M.A.; Hayhurst, A.N.; Scott, S.A.; Dennis, J.S. Kinetics of the reduction of wüstite by hydrogen and carbon monoxide for the chemical looping production of hydrogen. *Chem. Eng. Sci.* **2014**, *120*, 149–166. [CrossRef]
28. Berger, C.M. Sauerstoffspeicher für die Oxidkeramische Batterie: Herstellung, Charakterisierung und Betriebsverhalten. Ph.D. Thesis, Ruhr-Universität Bochum, Bochum, Germany, 2016.
29. Braun, W. Ermittlung thermochemischer und kinetischer Daten an Speichermaterialien zur Verwendung in einer oxidkeramischen Batterie. Ph.D. Thesis , Rheinisch-Westfälischen Technischen Hochschule Aachen, Aachen, Germany, 2017.
30. Huber, L.; Gamisch, B.; Dawoud, B. Experimental Investigation of the Cycle Stability of different Iron Oxide Composites for a Redox Hydrogen Storage Process. In Proceedings of the International Renewable Energy Storage Conference 2021 (IRES 2021), Online, 16–18 March 2021. [CrossRef]
31. Böhm, A.; Plochberger, T. Grundsätzliches zum Pelletieren und Versuchstechnik am Beispiel Eisenerzpelletierung. *BHM Berg-und Hüttenmännische Monatshefte* **2010**, *155*, 249–256. [CrossRef]

32. de Moraes, S.L.; de Lima, J.R.B.; Ribeiro, T.R. Iron Ore Pelletizing Process: An Overview. In *Iron Ores and Iron Oxide Materials*; IntechOpen: London, UK, 2018. [CrossRef]
33. Sastry, K.; Fuerstenau, D.W. Mechanisms of agglomerate growth in green pelletization. *Powder Technol.* **1973**, *7*, 97–105. [CrossRef]
34. Schubert, H. *Handbuch der Mechanischen Verfahrenstechnik*; John Wiley & Sons: Hoboken, NJ, USA, 2005; pp. 433–464. [CrossRef]
35. Schwister, K.; Leven, V. *Verfahrenstechnik für Ingenieure: Lehr- und Übungsbuch*, 4th ed.; Hanser: München, Germany, 2020. [CrossRef]
36. Mallya, S.; Lam, E. *White and Pharoah's Oral Radiology*, 8th ed.; Elsevier: Amsterdam, The Netherlands, 2019.
37. Berger, C.M.; Tokariev, O.; Orzessek, P.; Hospach, A.; Fang, Q.; Bram, M.; Quadakkers, W.J.; Menzler, N.H.; Buchkremer, H.P. Development of storage materials for high-temperature rechargeable oxide batteries. *J. Energy Storage* **2015**, *1*, 54–64. [CrossRef]
38. Kim, S.H.; Zhang, X.; Ma, Y.; Souza Filho, I.R.; Schweinar, K.; Angenendt, K.; Vogel, D.; Stephenson, L.T.; El-Zoka, A.A.; Mianroodi, J.R.; et al. Influence of microstructure and atomic-scale chemistry on the direct reduction of iron ore with hydrogen at 700 °C. *Acta Mater.* **2021**, *212*, 116933. [CrossRef]
39. Spreitzer, D.; Schenk, J. Reduction of Iron Oxides with Hydrogen—A Review. *Steel Res. Int.* **2019**, *90*. [CrossRef]
40. Higuhi, K.; Heerema, R.H. Influence of Artificially Induced Porosity on Strength and Reduction Behavior of Hematite Compacts. *ISIJ Int.* **2005**, *45*, 574–581. [CrossRef]

Disclaimer/Publisher's Note: The statements, opinions and data contained in all publications are solely those of the individual author(s) and contributor(s) and not of MDPI and/or the editor(s). MDPI and/or the editor(s) disclaim responsibility for any injury to people or property resulting from any ideas, methods, instructions or products referred to in the content.